Silesian University of Technology
Faculty of Mechanical Engineering
Department of Engineering Materials and Biomaterials

Extended Abstract of the Doctoral Dissertation

Material characterization of SLM-printed duplex stainless steel

Badania własności stali nierdzewnej typu duplex drukowanej technologią SLM

Candidate: Mengistu Jemberu Dagnaw, M.Sc.
Supervisor: Zbigniew Brytan, PhD, DSc Eng.
Academic discipline: Materials Engineering
Place and year: Gliwice, Poland, 2026

1 Research background and scientific context

LPBF enables near-net-shape fabrication of stainless-steel components with complex geometries, but it also imposes a thermal history that is fundamentally different from wrought processing [4]. In super duplex stainless steel 2507, the problem is severe because the engineering value of the alloy depends on a controlled ferrite–austenite constitution [1, 2]. Ferrite contributes strength and resistance to chloride stress-corrosion cracking, whereas austenite improves ductility, toughness, and strain accommodation [1, 3]. A dense additively manufactured part is therefore not automatically a metallurgically acceptable duplex stainless steel.

The dissertation treats LPBF-fabricated SDSS 2507 as a non-equilibrium metallurgical state. Rapid solidification, steep thermal gradients, cyclic reheating, melt-pool overlap, residual stress, cellular/subcellular structures, local segregation, texture, and defects jointly determine the starting material state [4, 5, 7]. The central scientific problem is not simply whether SDSS 2507 can be printed; it is whether the inherited LPBF phase–defect state can be controlled by heat treatment and Ni modification to obtain useful combinations of phase balance, mechanical performance, and laboratory electrochemical response.

This framing prevents density-based overinterpretation. Porosity control is necessary, but low porosity does not prove duplex recovery, chemical homogenization, benign residual stress, absence of nanoscale decomposition, or localized-corrosion resistance. The dissertation is therefore organized around a processing–microstructure–mechanical–electrochemical pathway rather than around one isolated processing variable.

The conceptual structure of the dissertation is summarized in Figure 1. The figure shows how LPBF processing produces a non-equilibrium phase–defect state, which is then modified by Ni addition and post-build heat treatment before being evaluated through microstructural, mechanical, electrochemical, and descriptor-level screening evidence.

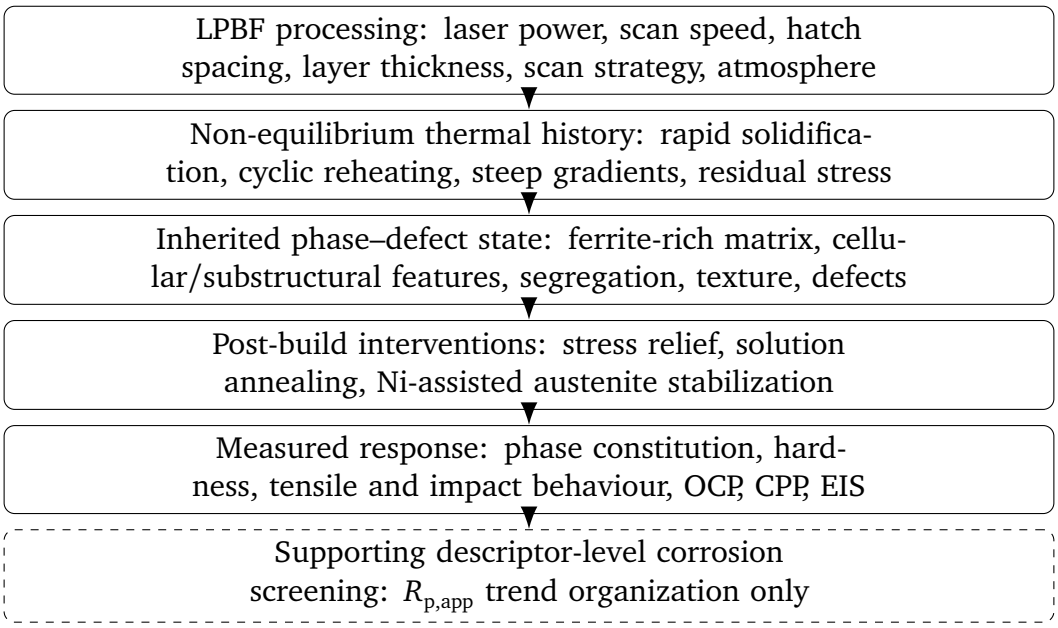

Figure 1: Conservative framework used in the extended abstract. The corrosion-screening block is not treated as independent validation of localized-corrosion resistance.

This framework defines the interpretation boundary of the extended abstract: the corrosion-

screening workflow is treated as a supporting descriptor-level layer, while the primary evidence comes from direct characterization, mechanical testing, CPP, and EIS.

2 Research gap and justification

The literature identifies four linked gaps that motivate this dissertation. First, LPBF-fabricated duplex and super duplex stainless steels are often evaluated primarily through densification and strength, although their engineering suitability also depends on ferrite–austenite phase balance, defect morphology, residual-strain indicators, crystallographic texture, local chemistry, secondary-phase susceptibility, and corrosion response [5, 7]. High relative density is therefore necessary but not sufficient to demonstrate metallurgical suitability.

Second, post-build stress relief and solution annealing are frequently interpreted using concepts developed for wrought or welded SDSS [1, 3]. This transfer is incomplete because LPBF produces a distinct starting condition: a ferrite-rich, chemically heterogeneous, defect-containing, textured, and residually strained microstructure [4, 7]. The response to heat treatment must therefore be evaluated from the LPBF-inherited phase–defect state rather than assumed from conventional SDSS behaviour.

Third, Ni addition is commonly treated as a straightforward austenite-stabilising strategy. While Ni can promote austenite formation, its effect in LPBF-fabricated SDSS 2507 is not automatically beneficial because phase balance, phase connectivity, heat treatment, and local chemistry modify the final response [1, 3, 7]. Excessive Ni enrichment may shift the alloy toward austenite-rich rather than balanced duplex states and may change strength, ductility, impact response, phase connectivity, and electrochemical behaviour in a criterion-dependent manner.

Fourth, data-driven corrosion screening can support trend organisation across composition, processing, heat treatment, and electrochemical descriptors, but it cannot replace direct OCP, CPP, EIS, or post-corrosion evidence [8, 9]. Model-derived descriptors require a defined applicability domain and must be treated as supporting indicators rather than independent proof of localized-corrosion resistance.

The study is therefore justified by the need to assess LPBF-fabricated SDSS 2507 as a coupled processing–structure–property–corrosion system. Its scientific value lies in identifying pathway-specific behaviour across standard, +3 wt.% Ni, and +6 wt.% Ni alloy variants, rather than claiming a single universal optimum based on density, Ni content, heat-treatment temperature, or one isolated performance metric.

3 Aim, thesis statement, and working hypotheses

The dissertation aims to determine how post-build heat treatment and deliberate Ni modification affect the LPBF-inherited microstructure, mechanical response, and electrochemical behaviour of SDSS 2507. Standard UNS S32750/SDSS 2507, SDSS 2507 +3 wt.% Ni, and SDSS 2507

+6 wt.% Ni are compared using a common LPBF processing basis and alloy-specific heat-treatment pathways. The main scientific thesis of the dissertation is:

> *The performance of LPBF-fabricated SDSS 2507 is governed by the coupled phase–defect–strain state generated by alloy chemistry, LPBF thermal history, and post-build treatment. Ni addition and heat treatment can shift ferrite–austenite balance and material response, but the optimum processing pathway is criterion-specific rather than universal.*

This formulation is deliberately bounded. It avoids overclaiming monotonic benefits from Ni addition, universal corrosion improvement, or service-level qualification from laboratory electrochemical screening alone. The dissertation evaluates three working hypotheses, denoted as H1–H3, where "H" refers to a working hypothesis:

H1. **Ni-assisted austenite-stabilisation hypothesis.** Deliberate Ni addition shifts the as-built LPBF phase constitution toward increased austenite formation relative to the standard alloy, but excessive Ni may produce austenite-rich rather than balanced duplex states.

H2. **Post-build thermal-pathway hypothesis.** Stress relief and solution annealing modify the LPBF-inherited phase–defect state through different thermal pathways. Stress relief mainly modifies the retained ferrite-rich inherited state, whereas solution annealing provides stronger ferrite–austenite rebalancing.

H3. **Coupled phase–defect–response hypothesis.** Mechanical and electrochemical responses depend on the coupled phase constitution, defect state, orientation heterogeneity, local chemistry, and heat-treatment condition, rather than on porosity, nominal Ni content, or treatment temperature alone.

4 Research scope and interpretation limits

The study covers LPBF-fabricated standard SDSS 2507 and two experimentally Ni-modified variants. The investigated domain includes the as-built condition, selected stress-relief treatments, and selected solution-annealing treatments. The electrochemical environment is naturally aerated 3.5 wt.% NaCl at 25 °C. The analysis includes SEM, XRD, EBSD, selected TEM/STEM, hardness, tensile testing, unnotched Charpy impact testing, OCP, CPP, EIS, and a bounded $R_{p,app}$-based screening workflow.

The scope is not factorial. The heat-treatment schedules are alloy-specific; therefore, cross-alloy comparisons are pathway comparisons, not direct composition–temperature–time factorial comparisons. The dissertation also does not establish fatigue resistance, stress-corrosion cracking resistance, crevice-corrosion resistance, critical pitting temperature, quantitative pit-depth statistics, rough as-built surface corrosion performance, service-life prediction, or component-scale qualification. These omissions are not cosmetic. They define the boundary between defensible laboratory screening and overstatement.

5 Materials and experimental design

Three feedstock systems were investigated: standard SDSS 2507, SDSS 2507 +3 wt.% Ni, and SDSS 2507 +6 wt.% Ni. The modified powders were prepared by blending the standard 2507-type powder with pure Ni powder. Because powder blending can retain local heterogeneity, the Ni-modified alloys should be treated as experimental compositional variants rather than direct commercial UNS S32750 equivalents.

The nominal compositions of the three investigated powder systems are summarized in Table 1. The progressive increase in Ni content was used to shift the ferrite–austenite stability balance, while the associated changes in Cr, Mo, and N were retained in the interpretation of phase constitution and corrosion response.

Table 1: Nominal compositions of the investigated powder systems, wt.%.

Alloy	Fe	Cr	Ni	Mo	Mn	Si	N	Cu	C	P	S	O
Standard SDSS 2507	Bal.	25.0	6.3	3.8	0.4	0.35	0.30	0.15	0.016	0.024	0.001	0.017
SDSS 2507 +3 wt.% Ni	Bal.	24.4	9.1	3.7	0.4	0.29	0.30	0.14	0.016	0.023	0.001	0.016
SDSS 2507 +6 wt.% Ni	Bal.	23.7	11.9	3.6	0.4	0.28	0.30	0.14	0.015	0.023	0.001	0.016

The selected LPBF condition was $P = 180\,\mathrm{W}$, $v = 300\,\mathrm{mm\,s^{-1}}$, $h = 120\,\mu\mathrm{m}$, and $t = 30\,\mu\mathrm{m}$, corresponding to $V_{\mathrm{ED}} = 166.7\,\mathrm{J\,mm^{-3}}$. As shown in Figure 2, the porosity-based process-window screening supports the selection of this condition as a common low-porosity processing basis. However, this selection should not be interpreted as an optimized metallurgical condition for all phase, mechanical, and corrosion criteria.

Specimens for metallography and electrochemical testing were sectioned from printed coupons along defined build-related planes where relevant, mounted in epoxy resin, ground using SiC papers, polished using diamond suspensions and colloidal silica, and electrolytically etched in oxalic-acid solution for microstructural examination. The exposed area and final surface preparation were kept consistent for electrochemical comparisons. This information is included because surface preparation and section orientation can affect SEM/EBSD quality and corrosion descriptors.

The alloy-specific post-build heat-treatment matrix is given in Table 2; FC denotes furnace cooling and WQ denotes water quenching. Because the heat-treatment schedules were not fully factorial across the three alloy systems, comparisons among alloys are interpreted as pathway-based trends rather than direct temperature–time–composition effects.

Table 2: Alloy-specific heat-treatment matrix.

Alloy system	Condition	Temperature	Time	Cooling/class
Standard SDSS 2507	AS	–	–	As-built
	SR300	300 °C	5 h	FC, stress relief
	SR400	400 °C	1 h	FC, stress relief
	SR550	550 °C	5 h	FC, stress relief

Alloy system	Condition	Temperature	Time	Cooling/class
	SA1100	1100 °C	15 min	WQ, solution annealing
SDSS 2507 +3 wt.% Ni	AS	–	–	As-built
	SR400	400 °C	1 h	FC, stress relief
	SR450	450 °C	1 h	FC, stress relief
	SR500	500 °C	1 h	FC, stress relief
	SR550	550 °C	1 h	FC, stress relief
	SA1100	1100 °C	15 min	WQ, solution annealing
SDSS 2507 +6 wt.% Ni	AS	–	–	As-built
	SR350	350 °C	2 h	FC, stress relief
	SR425	425 °C	1 h	FC, stress relief
	SR525	525 °C	1 h	FC, stress relief
	SA1150	1150 °C	10 min	WQ, solution annealing

6 Research methods

The methodology was multi-technique by design. SEM was used for morphology and defect-related observations; XRD for phase identification and comparative peak-broadening descriptors; EBSD for mapped phase fractions, grain morphology, orientation relationships, boundary descriptors, KAM, GROD, GOS, and texture descriptors; TEM/STEM/SAED/STEM-EDS for selected nanoscale assessment; hardness, tensile, and unnotched Charpy testing for mechanical response; OCP, CPP, and EIS for electrochemical response; and a $R_{p,app}$-based machine-learning workflow for bounded corrosion-response trend organization.

XRD was used with the Williamson–Hall framework as a descriptor-level approach for comparative peak broadening, not as an absolute residual-stress or dislocation-density measurement [10]. EBSD boundary descriptors were interpreted using crystallographic boundary concepts, including near-CSL classification where appropriate [11]. OCP, CPP, and EIS were interpreted as laboratory electrochemical descriptors, with localized-corrosion claims bounded by the limits of electrochemical testing and pitting-corrosion interpretation [8, 9].

The main characterization and testing methods, together with their conservative interpretation limits, are summarized in Table 3. This boundary is important because no single method alone can establish phase balance, nanoscale precipitation state, mechanical performance, and corrosion resistance.

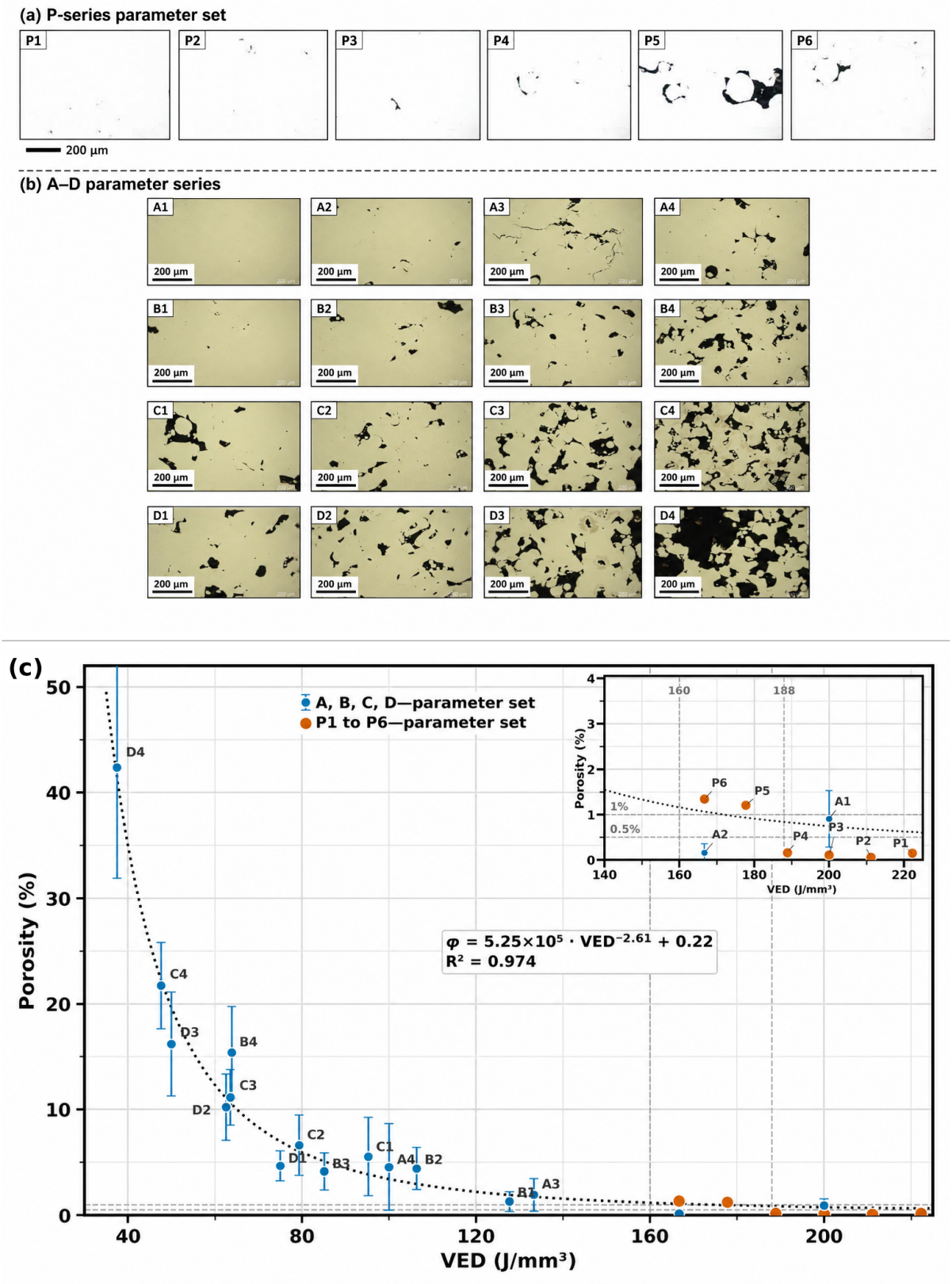

Figure 2: Porosity-based LPBF process-window screening for SDSS 2507: **(a)** P1–P6 preheated parameter set, **(b)** A–D parameter series, and **(c)** porosity area fraction versus volumetric energy density. The figure supports selection of a common low-porosity LPBF condition, but does not establish metallurgical, mechanical, or corrosion suitability.

Table 3: Methods and conservative interpretation boundaries.

Method	Evidence provided	Interpretation limit
SEM/EDS	Microstructure, melt-pool/defect features, micron-scale chemistry	Limited for nanoscale precipitates and nitrogen-sensitive chemistry.
XRD	Phase identification and comparative peak broadening	Not absolute residual stress, dislocation density, or phase fraction without rigorous correction/refinement.
EBSD	Mapped phase fraction, texture, misorientation, and boundary descriptors	Area-specific; not full-volume phase balance or absolute stored energy.
TEM/STEM	Selected nanoscale/substructural evidence	Local; absence of precipitates in one region is not global absence.
Mechanical testing	Hardness, tensile response, and unnotched impact response	Test geometry and orientation matter; unnotched Charpy energies are comparative only.
OCP/CPP/EIS	Laboratory electrochemical descriptors	Not service-level corrosion qualification without pit statistics, CPT, or long-term exposure.
ML screening	Descriptor-level trend organization	Not transferable prediction or independent corrosion validation.

7 Main results

The selected LPBF parameter set provided a common low-porosity processing basis for comparing alloy and heat-treatment effects. This processing baseline was necessary for cross-condition comparison, but it did not by itself ensure restoration of a balanced duplex microstructure. The feedstocks were predominantly spherical, with satellite particles and local irregularities. The +6 wt.% Ni feedstock showed a modest shift toward coarser particle size relative to the standard and +3 wt.% Ni feedstocks, and this was treated as a possible feedstock-level variable in cross-alloy interpretation.

The phase-constitution results showed that the standard and +3 wt.% Ni alloys remained strongly ferrite-rich after LPBF and stress relief. Solution annealing at 1100 °C produced approximately balanced mapped phase fractions in the standard alloy, with 50.9% α-Fe and 49.1% γ-Fe. In contrast, the +3 wt.% Ni alloy became austenite-rich after SA1100, with 69.4% γ-Fe. The +6 wt.% Ni alloy showed higher mapped austenite fractions already in the as-built and stress-relieved states: 52.1% γ-Fe in AS, 54.2% after SR350 and SR425, 60.8% after SR525, and 89.1% after SA1150. These results show that Ni addition promoted austenite stabilisation, but not in a universally beneficial or monotonic manner. In particular, the +6 wt.% Ni SA1150 state overshot the duplex target and became strongly austenite-rich.

The mapped-area phase-balance pathway is summarized in Figure 3. The figure is used as the principal EBSD phase-fraction evidence in the extended abstract because it compares the as-built and solution-annealed endpoints across the standard, +3 wt.% Ni, and +6 wt.% Ni alloy systems without overloading the text with the full EBSD map series.

The EBSD boundary and orientation-relationship analyses supported a transformation-controlled interpretation of austenite reformation. For the +3 wt.% Ni alloy, SA1100 increased the same-phase $\Sigma 3$ boundary-length fraction and produced ferrite–austenite interphase-boundary misorientation populations compatible with transformation-related Kurdjumov–Sachs and Nishiyama–Wassermann orientation relationships. KAM, GROD, and GOS trends were consistent with reduced local orientation heterogeneity after solution annealing. These EBSD

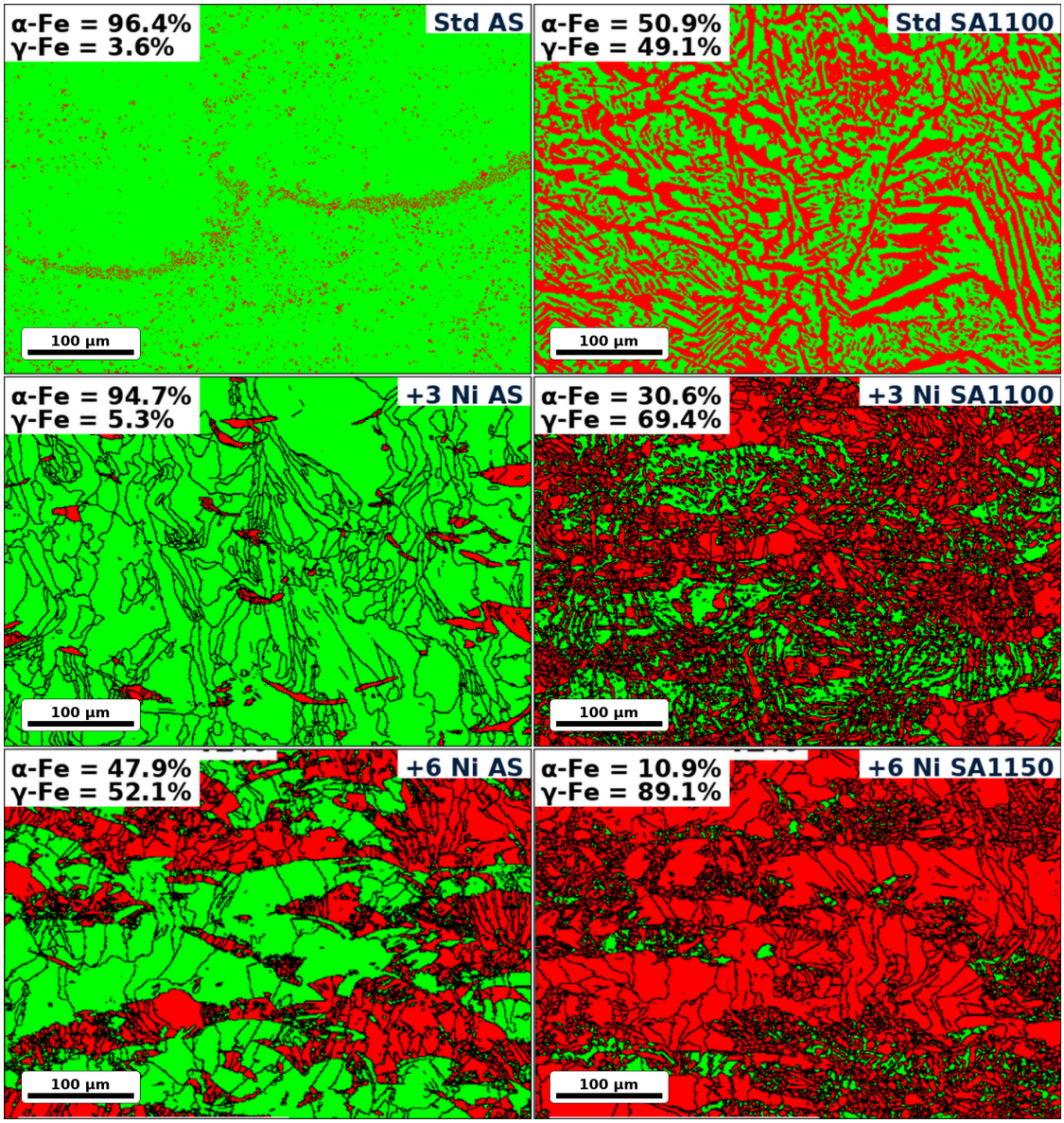

Figure 3: EBSD phase-balance pathway for selected standard, +3 wt.% Ni, and +6 wt.% Ni LPBF-fabricated SDSS 2507 conditions. The maps compare ferrite-rich, near-duplex, and austenite-rich states using mapped-area phase fractions. The values are EBSD mapped-area descriptors and should not be interpreted as full-build volumetric phase fractions.

quantities were used as comparative descriptors of orientation heterogeneity, not as direct residual-stress measurements.

The XRD results did not show a universal recovery trend. The standard alloy showed reduced ferrite peak-broadening descriptors after stress relief, whereas the Ni-modified alloys responded non-monotonically. In the +6 wt.% Ni alloy, SR425 gave the strongest broadening increase, while SR525 showed the highest KAM-based orientation heterogeneity. The stacked +6 wt.% Ni XRD patterns in Figure 4 provide the phase-identification context for the AS, SR350, SR425, SR525, and SA1150 conditions; they are used here as qualitative reflection evidence for ferrite/austenite evolution, not as a replacement for EBSD-based mapped-area phase-fraction analysis. The results therefore do not support a simplified interpretation in which increasing heat-treatment temperature necessarily produces progressive recovery. TEM/STEM analysis of the standard SR550 condition showed ferritic nanoscale/substructural contrast, but sigma, chi, or chromium nitride precipitates were not confirmed in the analysed region by the applied TEM/STEM, SAED, and STEM-EDS evidence. This observation is restricted to the selected analysed region and the detection limits of the applied methods.

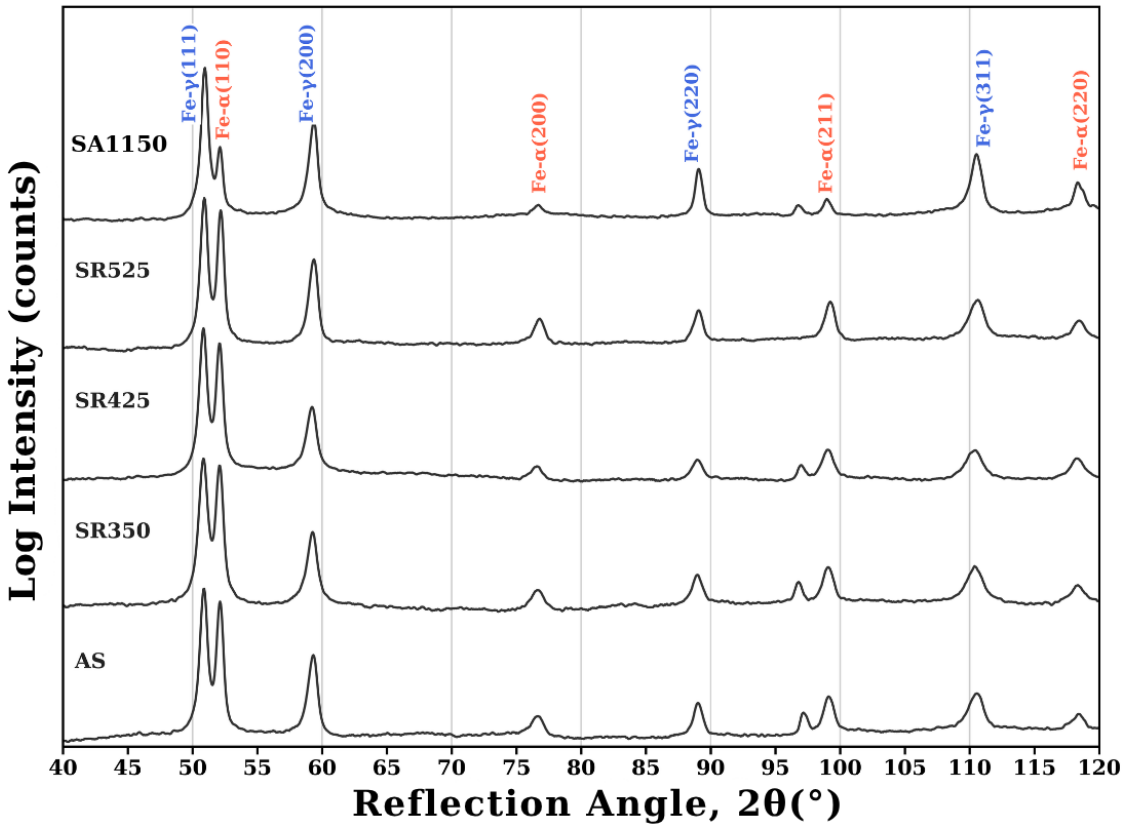

Figure 4: XRD patterns of the LPBF-fabricated SDSS 2507 +6 wt.% Ni alloy in the AS, SR350, SR425, SR525, and SA1150 conditions. Ferritic and austenitic reflections are labelled as α-Fe and γ-Fe, respectively. The patterns provide qualitative phase-identification evidence and should not be interpreted as quantitative phase-fraction measurements.

The mechanical response followed a strength–ductility–impact trade-off. As-built and stress-relieved states retained higher hardness and strength, whereas solution annealing improved elongation and impact response with an associated reduction in strength. The +3 wt.% Ni SR400/SR450 route gave the highest tensile-strength pathway, reaching approximately 1414 MPa. Solution-annealed states were favoured for ductility and impact-energy response, while selected +6 wt.% Ni AS/SR states provided a strong non-solution-annealed compromise

between ductility and impact response. These trends indicate that the optimum condition depends on the selected mechanical criterion. The high strength of the as-built and stress-relieved states is consistent with ferrite-rich phase constitution, LPBF-derived refinement, and retained orientation/strain heterogeneity. In contrast, solution annealing promoted austenite-mediated strain accommodation and improved comparative elongation and unnotched impact response, but reduced the strengthening contribution inherited from the LPBF condition.

The tensile-strength pathway is visualized in Figure 5. The figure is included to make the strength penalty of solution annealing and the strength advantage of the +3 wt.% Ni SR400/SR450 route explicit. The values should be read as comparative tensile results within the investigated specimen geometry and processing matrix.

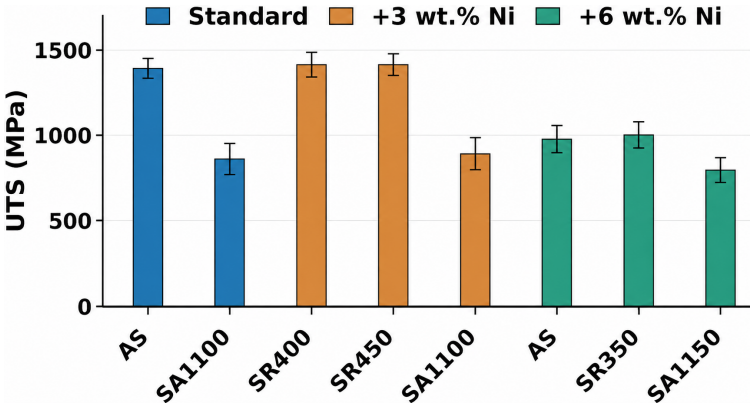

Figure 5: Ultimate tensile strength summary for selected LPBF-fabricated SDSS 2507 alloy–condition pathways. The plot highlights the high-strength response of as-built/stress-relieved states and the strength reduction after solution annealing. Error bars represent the plotted data dispersion available for the tensile dataset.

The electrochemical ranking also depended on the selected descriptor. J_{corr}, R_p, E_{br}, E_{rp}, and EIS-derived R_{ct} did not identify one universal optimum. The favoured pathways were standard SR400 within the standard alloy, +3 wt.% Ni SR500/SR550 for CPP-based descriptors, +3 wt.% Ni SR450/SR550 for EIS-derived R_{ct}, +6 wt.% Ni SR350 for breakdown/repassivation descriptors, and +6 wt.% Ni SR525 for resistance-related descriptors. These results are laboratory electrochemical descriptor rankings; they do not demonstrate long-term service corrosion resistance, pitting immunity, crevice-corrosion resistance, stress-corrosion-cracking resistance, or critical-pitting-temperature performance. Representative electrochemical evidence for the +6 wt.% Ni alloy is shown in Figure 6. The SR350 CPP response is used to represent the breakdown/repassivation descriptor pathway, whereas the SR525 EIS response represents the resistance-related pathway. These plots are representative electrochemical traces/descriptors, not statistical proof of service corrosion durability.

The machine-learning corrosion-screening workflow showed close internal agreement for the $R_{p,app}$ descriptor, with $R^2 = 0.9786$, MAE $= 0.0025$, and RMSE $= 0.0040$. Ni, Cr, Mo, PREN, heat-treatment, processing, and environment descriptors influenced the predicted response, with Ni showing a nonlinear effect. However, the +3 wt.% Ni records were part of the training domain; therefore, these metrics represent internal consistency rather than external validation. The workflow is useful as descriptor-level trend organisation, not as a standalone corrosion predictor. The corrosion-screening architecture and predicted descriptor projections are shown in Figure 7. The figure is included only to document how the descriptor-level $R_{p,app}$ trends

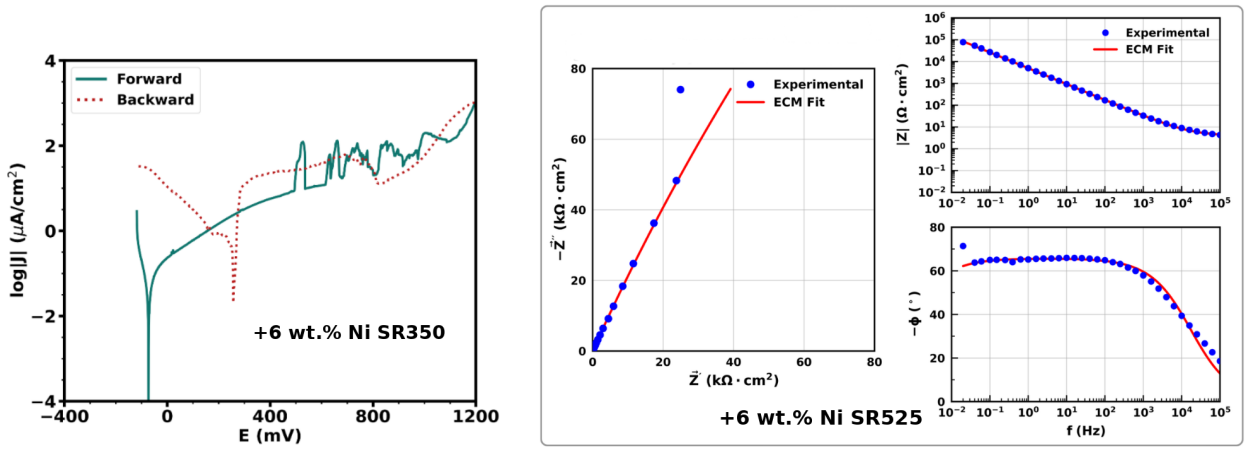

(a) +6 wt.% Ni SR350 CPP **(b)** +6 wt.% Ni SR525 EIS

Figure 6: Representative electrochemical responses for selected +6 wt.% Ni conditions: **(a)** CPP trace for SR350, used as the representative breakdown/repassivation-descriptor pathway, and **(b)** EIS Nyquist/Bode response for SR525, used as the representative resistance-related pathway. The EIS fit is used as a comparative descriptor and remains model-dependent.

were organized; it must not be read as direct evidence of passive-film chemistry, phase-resolved corrosion behaviour, or external predictive validity.

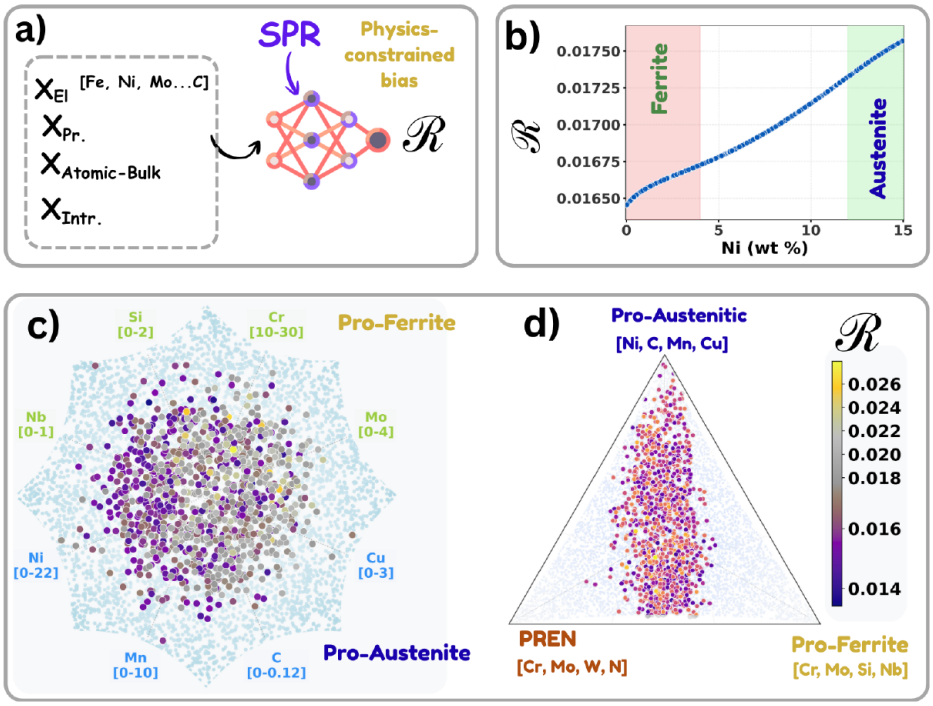

Figure 7: Model architecture and screening-level corrosion-response trends: **(a)** neural network architecture, **(b)** conditional Ni-response projection, **(c)** alloying-element projection, and **(d)** PREN–SPER triangular projection. Marker colour represents the predicted $R_{p,app}$. This figure is reproduced from the dissertation's corrosion-screening section and is interpreted only as descriptor-level screening evidence.

The criterion-specific condition-selection logic derived from the experimental results is summarized in Table 4. The table separates phase balance, strength, ductility, impact response, CPP-derived descriptors, EIS-derived resistance indicators, and screening descriptors to avoid implying a single universal optimum.

Table 4: Criterion-specific pathway-selection summary for the investigated LPBF SDSS 2507 alloy conditions.

Selection criterion	Favoured pathway	Conservative basis
Phase rebalancing	Standard SDSS 2507 SA1100	Closest recovery toward balanced EBSD-mapped ferrite–austenite constitution.
Maximum tensile strength	SDSS 2507 +3 wt.% Ni SR400/SR450	Highest strength-oriented pathway; ferrite-rich LPBF-inherited state retained.
Ductility	Solution-annealed states	Improved elongation relative to high-strength as-built and stress-relieved states.
Unnotched impact response	Solution-annealed states and selected +6 wt.% Ni AS/SR states	Better comparative impact response; not standard Charpy V-notch toughness.
Breakdown and repassivation descriptors	SDSS 2507 +6 wt.% Ni SR350	Favoured CPP-derived breakdown/repassivation behaviour.
Resistance-related descriptors	SDSS 2507 +6 wt.% Ni SR525	Favoured resistance-related CPP/EIS trends.
Balanced CPP response in +3 wt.% Ni	SDSS 2507 +3 wt.% Ni SR500	Most balanced CPP-based screening response within the +3 wt.% Ni set.

8 Integrated discussion

The results support the working hypotheses within the investigated domain. Ni addition shifted the phase constitution toward austenite, consistent with duplex stainless-steel phase-stability principles [1, 3], but the effect was not linearly beneficial under the investigated LPBF conditions. Stress relief modified the inherited LPBF state without reliably restoring duplex balance, whereas solution annealing provided the strongest austenite restoration, consistent with recent LPBF/PBF-LB SDSS heat-treatment evidence [6, 7]. Mechanical and electrochemical responses depended on the combined phase–defect–strain state rather than on any single variable. The strongest scientific argument of the dissertation is the pathway concept. The material is not classified by composition alone; it is classified by the route that produced the measured phase constitution, orientation heterogeneity, defect state, mechanical response, and electrochemical descriptors. This is why the thesis identifies multiple preferred conditions instead of a single winner. Standard SA1100 is appropriate for phase-balance recovery within the investigated matrix. The +3 wt.% Ni SR400/SR450 route is appropriate for maximum tensile strength. The +6 wt.% Ni SR350 and SR525 states are favoured for different electrochemical descriptors. Solution annealing is favoured for ductility and impact response, but not for strength retention. The corrosion-screening model is therefore interpreted only as a descriptor-level support tool. It does not prove service corrosion resistance. Similarly, the absence of confirmed sigma, chi, or chromium nitride precipitates in the selected TEM/STEM region does not prove global absence of nanoscale precipitation. These boundaries preserve the distinction between direct evidence, interpretation, and extrapolation.

9 Hypothesis verification

The research hypotheses were supported within the investigated experimental domain.

H1 was supported because Ni addition increased the EBSD-mapped austenite fraction in the investigated LPBF-fabricated SDSS 2507 variants. However, the +6 wt.% Ni SA1150 condition became strongly austenite-rich, confirming that excessive Ni addition may shift the alloy beyond the desired duplex phase balance.

H2 was supported because stress relief modified the LPBF-inherited phase–defect state but did not reliably restore duplex phase balance, whereas solution annealing produced the strongest ferrite–austenite rebalancing within the investigated heat-treatment matrix.

H3 was supported because the mechanical and electrochemical responses were criterion-dependent. They were governed by the coupled phase constitution, defect state, orientation heterogeneity, local chemistry, and heat-treatment pathway, not by porosity, nominal Ni content, or heat-treatment temperature alone.

Therefore, the main research objective was achieved. The dissertation determined how Ni modification and post-build heat treatment affect the LPBF-inherited microstructure, mechanical response, and laboratory electrochemical behaviour of SDSS 2507. It also established a criterion-specific framework for selecting alloy–heat-treatment pathways within the investigated experimental domain.

10 Main conclusions

1. The selected LPBF condition provided a common low-porosity processing basis for comparing the investigated alloy–heat-treatment pathways. However, low porosity alone did not establish duplex phase balance, microstructural suitability, or corrosion suitability.

2. Phase constitution was strongly alloy- and treatment-dependent. The standard and +3 wt.% Ni alloys remained ferrite-rich after LPBF and stress relief, whereas solution annealing was required for substantial ferrite–austenite rebalancing. The +6 wt.% Ni alloy increased the mapped austenite fraction substantially, including near-duplex AS/SR states, but SA1150 produced a strongly austenite-rich mapped phase constitution.

3. Stress relief did not produce a universal recovery trend. XRD and EBSD descriptors showed alloy-specific and non-monotonic responses, while TEM/STEM of the standard SR550 condition did not confirm sigma, chi, or chromium nitride precipitates in the analysed region. This nanoscale observation is local and does not prove global absence of such features.

4. The mechanical and electrochemical responses were criterion-dependent. As-built and stress-relieved states favoured strength retention, whereas solution annealing favoured ductility and impact response with strength reduction. CPP and EIS descriptors did not identify a single universal electrochemical optimum.

5. The main contribution is a criterion-specific pathway map linking LPBF processing, Ni modification, heat treatment, phase constitution, mechanical response, laboratory electrochemical descriptors, and bounded $R_{p,app}$-based screening. The machine-learning workflow should be interpreted only as a dataset-specific trend-organization tool, not as service validation or a transferable corrosion predictor.

11 Original scientific contribution

The original contribution of this dissertation is not the identification of a single Ni level or heat treatment that universally optimizes LPBF-fabricated SDSS 2507. Its contribution is the development of a process-specific and evidence-bounded framework for selecting alloy–heat-treatment pathways according to the dominant performance criterion. The work demonstrates that phase balance, strength, ductility, impact response, electrochemical descriptors, and screening-model outputs do not converge toward one universal optimum. Instead, each response is governed by the coupled effects of alloy chemistry, LPBF thermal history, post-build treatment, phase constitution, defect state, orientation heterogeneity, and local chemistry. The dissertation contributes the following original elements:

- Comparative assessment of standard SDSS 2507, SDSS 2507 +3 wt.% Ni, and SDSS 2507 +6 wt.% Ni fabricated using a common LPBF processing basis.
- Clarification that Ni-assisted austenite stabilisation in LPBF SDSS 2507 is criterion-dependent and may shift the alloy beyond the desired duplex balance under high-temperature solution annealing.
- Integrated processing, structure, property, and corrosion interpretation based on SEM, XRD, EBSD, TEM/STEM, hardness, tensile testing, impact testing, CPP, EIS, and descriptor-level modelling.
- Criterion-specific pathway-selection map separating phase rebalancing, maximum tensile strength, ductility, impact response, CPP-derived descriptors, EIS resistance indicators, and corrosion-screening descriptors.
- Bounded use of machine learning as a descriptor-level corrosion trend-organisation tool, while retaining direct electrochemical testing as the primary corrosion evidence.

12 Practical and engineering significance

The practical significance of the dissertation is the development of a condition-selection logic for LPBF-fabricated SDSS 2507. Alloy and heat-treatment selection should be made according to the dominant engineering criterion, not by nominal Ni content or heat-treatment temperature alone. Within the investigated matrix, standard SDSS 2507 SA1100 is the most suitable route when phase-balance restoration is the priority. The +3 wt.% Ni SR400/SR450 pathway is the strongest route when maximum tensile strength is required. Solution-annealed states are more

appropriate when ductility and impact response are prioritized, while selected +6 wt.% Ni AS/SR states remain relevant as non-solution-annealed strength–ductility/impact compromises. For laboratory electrochemical response, the preferred pathway depends on whether the dominant criterion is breakdown/repassivation behaviour, resistance-related response, CPP-derived descriptors, or EIS-derived resistance indicators. The engineering output is therefore not a universal processing recipe, but a criterion-specific framework for selecting alloy–heat-treatment pathways.

13 Publications, patents, and candidate's own contribution

The dissertation is supported by journal articles and peer-reviewed conference outputs related to LPBF-fabricated duplex and super duplex stainless steels, post-build heat treatment, microstructure, mechanical response, corrosion behaviour, and descriptor-level corrosion screening. The scientific articles related to the dissertation are:

1. Dagnaw M., Poudel S., Król M., Brytan Z., "Post-process heat treatment design for tunable strength and toughness in L-PBF 2507 super duplex stainless steel," *Materialia*, 2026, Article no. 102799, doi: 10.1016/j.mtla.2026.102799.
2. Dagnaw M. J., Poudel S., Subedi U., Thapa R., Reimann Ł., Appiah A. N. S., Nuckowski P. M., Król M., Brytan Z., Moelans N., Kunwar A., "Integrating experiments and phase-field method through informatics for tailored corrosion performance of additively manufactured steel microstructures," *Metals and Materials International*, 2026, accepted; DOI assigned: 10.1007/s12540-026-02369-4.
3. Dagnaw M. J., Brytan Z., Cimbala D., Simkulet V., Fita S., "Microstructure and hardness distribution of laser powder bed fusion-produced AISI 2507 super duplex stainless steel," *Defect and Diffusion Forum*, 2026, vol. 448, pp. 125–130, doi: 10.4028/p-gmBT5y.
4. Snopiński P., Ardayfio B. N. A., Dagnaw M. J., Król M., Kotoul M., Brytan Z., "Effect of Ni addition on the phase balance and grain boundary character distribution in 2507 Super Duplex Stainless Steel fabricated via LPBF," *Symmetry*, 2026, vol. 18, no. 1, Article 198, pp. 1–14, doi: 10.3390/sym18010198.
5. Brytan Z., Dagnaw M. J., Bidulská J., Bidulský R., Muhamad M. R., "Post-processing effect on the corrosion resistance of super duplex stainless steel produced by laser powder bed fusion," *Materials*, 2024, vol. 17, no. 12, Article 2807, pp. 1–15, doi: 10.3390/ma17122807.
6. Dagnaw M. J., Brytan Z., Bidulská J., Bidulský R., "Corrosion evaluation of super duplex stainless steel made by LPBF," *Acta Metallurgica Slovaca*, 2024, vol. 30, no. 1, pp. 34–40, doi: 10.36547/ams.30.1.1999.

The dissertation-related peer-reviewed conference proceedings and conference-book chapters are:

1. Olszewska A., Wanczura W., Czajkowski K., Jagla B., Toman K., Knysh O., Kolšovský A., Dagnaw M. J., Brytan Z., Bidulská J., "Shaping the microstructure and properties of duplex

stainless steels manufactured via LPBF additive technology," *TalentDetector2025_Summer: International Students Scientific Conference*, 2025, Prace Katedry Materiałów Inżynierskich i Biomedycznych, pp. 358–365, ISBN 978-83-65138-44-6.

2. Brytan Z., Dagnaw M. J., "Heat treatment effects on LPBF duplex stainless steel corrosion resistance," *28th IFHTSE 2023 Congress*, Yokohama, Japan, 2024, International Federation for Heat Treatment & Surface Engineering, ISBN 9781713889533.

3. Brytan Z., Bidulska J., Dagnaw M. J., "Investigation of corrosion resistance in various heat-treated states of LPBF-produced SDSS," *27th International Seminar of Ph.D. Students, SEMDOK 2024*, Western Tatras–Zuberec, Slovak Republic, 2024, Zilinska Univerzita, pp. 15–20, ISBN 978-80-554-2076-9.

4. Dagnaw M. J., Brytan Z., "Exploring the potential of duplex stainless steels in additive manufacturing: composition, corrosion, and challenges," *TalentDetector2024_Winter: International Students Scientific Conference*, 2024, Prace Katedry Materiałów Inżynierskich i Biomedycznych, pp. 111–118, ISBN 978-83-65138-39-2.

5. Dagnaw M., Brytan Z., "3D printing of duplex stainless steels – possibilities and challenges," *TalentDetector2023_Winter: International Students Scientific Conference*, 2023, Prace Katedry Materiałów Inżynierskich i Biomedycznych, pp. 127–139, ISBN 978-83-65138-34-7.

6. Dagnaw M., Brytan Z., Bidulska J., Król M., Jonda E., Pastorek F., Kajanek D., "Initial optimization of L-PBF printing parameters of super duplex stainless steel powder," *26th International Seminar of Ph.D. Students, SEMDOK 2023*, Western Tatras–Zuberec, Slovak Republic, 2023, Zilinska Univerzita, pp. 70–75, ISBN 978-80-554-1947-3.

7. Dagnaw M., Brytan Z., "Microstructural and hardness distribution analysis of Laser Powder Bed Fusion (LPBF) printed 2507 duplex stainless steel," *TalentDetector2023_Summer: International Students Scientific Conference*, Brenna, Poland, 2023, Prace Katedry Materiałów Inżynierskich i Biomedycznych, pp. 193–200, ISBN 978-83-65138-38-5.

No patents are declared in the academic achievements, and no scientific monographs have been published by a listed publishing house, and no other chapters in scientific monographs beyond the conference-proceedings and conference-book chapters listed above. The candidate's own contribution consisted of designing and executing the comparative LPBF SDSS 2507 study; organizing the alloy and heat-treatment matrix; analyzing the microstructural, crystallographic, mechanical, and electrochemical datasets; developing and interpreting the bounded $R_{p,app}$-based screening workflow; preparing dissertation-related manuscripts and conference contributions; and synthesizing the processing, structure, property, and corrosion pathway map.

Key references

[1] R. N. Gunn, *Duplex Stainless Steels: Microstructure, Properties and Applications*. Woodhead Publishing, 1997.

[2] J.-O. Nilsson, “Super Duplex Stainless Steels,” *Materials Science and Technology*, vol. 8, no. 8, pp. 685–700, 1992.

[3] J. C. Lippold and D. J. Kotecki, *Welding Metallurgy and Weldability of Stainless Steels*. Wiley, 2005.

[4] T. DebRoy et al., “Additive manufacturing of metallic components – process, structure and properties,” *Progress in Materials Science*, vol. 92, pp. 112–224, 2018.

[5] X.-X. Zhu et al., “Laser Powder Bed Fusion of 2507 Duplex Stainless Steel: Microstructure, Mechanical Properties, and Corrosion Performance,” *Materials Science and Engineering: A*, vol. 913, p. 147084, 2024, doi: 10.1016/j.msea.2024.147084.

[6] A. D. Gandhi et al., “Solution Annealing of PBF-LB Manufactured 2507 Super Duplex Stainless Steel: A Computational Thermodynamics Approach,” *Welding in the World*, 2025, doi: 10.1007/s40194-025-02264-3.

[7] K. P. Davidson et al., “Effect of Build Orientation and Heat Treatment on the Microstructure, Mechanical and Corrosion Performance of Super Duplex Stainless Steels Fabricated via Laser Powder Bed Fusion,” *Materials Advances*, vol. 5, pp. 8177–8198, 2024, doi: 10.1039/D4MA00448E.

[8] G. S. Frankel, “Pitting corrosion of metals: a review of the critical factors,” *Journal of The Electrochemical Society*, vol. 145, no. 6, pp. 2186–2198, 1998.

[9] M. Stern and A. L. Geary, “Electrochemical polarization: I. A theoretical analysis of the shape of polarization curves,” *Journal of The Electrochemical Society*, vol. 104, no. 1, pp. 56–63, 1957.

[10] G. K. Williamson and W. H. Hall, “X-ray line broadening from filed aluminium and wolfram,” *Acta Metallurgica*, vol. 1, pp. 22–31, 1953.

[11] D. G. Brandon, “The structure of high-angle grain boundaries,” *Acta Metallurgica*, vol. 14, pp. 1479–1484, 1966.

List of abbreviations and symbols

AS	As-built condition	CPP	Cyclic potentiodynamic polarization
DSS	Duplex stainless steel	EBSD	Electron backscatter diffraction
EIS	Electrochemical impedance spectroscopy	EDS	Energy-dispersive X-ray spectroscopy
GOS	Grain orientation spread	GROD	Grain reference orientation deviation
KAM	Kernel average misorientation	LPBF	Laser powder bed fusion
OCP	Open-circuit potential	PREN	Pitting resistance equivalent number
SA	Solution-annealed condition	SDSS	Super duplex stainless steel
SEM	Scanning electron microscopy	SR	Stress-relieved condition
TEM/STEM	Transmission/scanning transmission electron microscopy	XRD	X-ray diffraction
E_{br}	Breakdown potential	E_{rp}	Repassivation potential
J_{corr}	Corrosion current density	R_{ct}	Charge-transfer resistance
R_p	Polarization resistance	$R_{p,app}$	Apparent CPP-derived screening descriptor